



**HAL**  
open science

# Understanding the Apparently Poor Conductivity of Galvanized Steel Plates

Andréa Cozza

► **To cite this version:**

Andréa Cozza. Understanding the Apparently Poor Conductivity of Galvanized Steel Plates. IEEE Access, 2021, 9, pp.146625 - 146639. 10.1109/ACCESS.2021.3123818 . hal-03410730

**HAL Id: hal-03410730**

**<https://centralesupelec.hal.science/hal-03410730>**

Submitted on 1 Nov 2021

**HAL** is a multi-disciplinary open access archive for the deposit and dissemination of scientific research documents, whether they are published or not. The documents may come from teaching and research institutions in France or abroad, or from public or private research centers.

L'archive ouverte pluridisciplinaire **HAL**, est destinée au dépôt et à la diffusion de documents scientifiques de niveau recherche, publiés ou non, émanant des établissements d'enseignement et de recherche français ou étrangers, des laboratoires publics ou privés.

---

# Understanding the Apparently Poor Conductivity of Galvanized Steel Plates

ANDREA COZZA<sup>1</sup>, (Senior Member, IEEE)

<sup>1</sup>GeePs, UMR CNRS - CentraleSupélec - Université Paris-Saclay - Sorbonne Universités, 3 rue Joliot-Curie, 91192 Gif-sur-Yvette, FRANCE. (e-mail: andrea.cozza@ieee.org)

Corresponding author: Andrea Cozza (e-mail: andrea.cozza@ieee.org).

⋮ **ABSTRACT** This paper investigates the physical reasons for the apparently poor conductivity of galvanized steel plates (GSP), which has not yet received a proper explanation. Apparent conductivities as low as 0.1 MS/m were reported in the past, which are incongruously low compared to the DC conductivity of steels (4 to 8 MS/m), or zinc (16.7 MS/m), the most common coating agent used against corrosion in steel products. A comprehensive review of results from metallurgy and materials science is presented, providing insights about the multi-layered structure of zinc-based coatings. These are found to be made of a limited set of intermetallic zinc-iron compounds each characterized by a steeply decreasing conductivity as their iron percentage increases. Depending on the galvanization process the relative thickness of these layers can vary widely, explaining the seemingly random apparent conductivity of GSP. Theoretical modeling of these structures shows that their apparent conductivity scales linearly with the frequency, suggesting that it can be far lower than acknowledged so far. An extensive analysis of power-dissipation data from the literature of GSP-based reverberation chambers confirms these predictions, with multiple instances of apparent conductivities as low as 10 kS/m. The conclusion is not that GSP are hopelessly poorly conductive, but rather that care should be taken in selecting the right coating technology, not only based on corrosion protection and minimizing costs, but also in view of its impact on GSP conductivity.

⋮ **INDEX TERMS** Apparent conductivity, galvanization, iron-zinc compounds, multi-layered structures, reverberation chamber, steel plate.

## I. INTRODUCTION

**S**TEEL plates find wide use as structural elements in many applications, such as in hangars, warehouses, ship hulls, cars and transportation vehicles, pipe lines and air ducts. In all of these applications steel is selected because of its superior mechanical strength, advantageous welding properties and low cost compared to other metals, rather than for its electrical properties.

With a DC conductivity ranging from about 4 to 8 MS/m, steel could be regarded as not necessarily such a bad conductor compared to the most common aluminum alloys, which have a typical conductivity around 20 MS/m [1]. In fact, right after the Second World War, experimental investigations with steel waveguides in the microwave range exposed conduction losses much higher than expected from its DC conductivity [2], [3], leading to the current use of copper and aluminum. More recently, the use of steel plates in a beam waveguide system in a Deep Space Network parabolic antenna led Otoshi to similar observations [4],

with apparent conductivities as low as 100 kS/m for structural steel plates. Subsequent investigations pointed to the fact that even when zinc plated, steel plates still displayed surprisingly low surface conductivities, about 4.4 MS/m compared to the expected 16.7 MS/m for zinc.

A poor surface conductivity has an especially strong impact in closed environments [5], where electromagnetic waves interact multiple times with metal surfaces, and in particular test facilities such as reverberation chambers (RC), which strongly rely on long reverberation times to build up high-strength fields for electromagnetic compatibility tests [6], [7]. Galvanized steel plates (GSP) used in typical RC are also zinc coated, but empirical results can be explained only by assuming that their surface conductivity be considerably lower than 1 MS/m [8], [9]. In all these previous empirical observations, no physical justification was advanced as to why GSP present such a low conductivity.

This paper addresses these questions by first discussing the physical structure of GSP coatings, reviewing results and

insights across metallurgy and materials science literature, where these topics are still actively researched [10]. As explained in Section II, the zinc layer initially applied to steel plates goes through complex metallurgy processes that significantly alter its physical and electrical properties. As a result, GSP coatings are far from being homogeneous structures, instead featuring multiple layers of iron-zinc (FeZn) compounds, each displaying a considerably different conductivity. The apparent conductivity of these structures is modeled in Section III, leading to the prediction that it should be significantly lower than that of the bulk conductivities of each layer. Partial interaction with the background magnetic steel plate is shown to be the main mechanism behind this phenomenon, resulting in a frequency-dispersive apparent conductivity.

Confirming these theoretical predictions requires wide-band testing of a large number of GSP, given the variability of GSP coatings. An effective solution is proposed in Section IV, by processing empirical insertion loss data available from RC literature. Clear evidence is presented supporting the previously discussed theoretical predictions: high variability across GSP samples, frequency dispersion and conductivities as low as 10 kS/m, lower than previously reported.

These results explain why the apparent conductivity of GSP changes significantly depending on the type of selected coating process and the frequency of operation. As discussed in Section V, this calls for joint considerations when selecting the most suitable GSP technology for a given application, taking into account not only corrosion-protection requirements and costs, but also how the physical structure of the coating would affect its apparent conductivity. It would be unnecessarily conservative and counterproductive to assume that GSP are inevitably bad conductors and that applications requiring good conductivity should switch to more expensive, lower yield-strength metals such as aluminum.

## II. WHAT LIES BENEATH GALVANIZING COATINGS?

Surface conductivity models of GSP developed in Section III require a detailed understanding of their physical structure and components. This section summarizes fundamental properties about galvanizing coatings, which are shown in Sections II-A and II-B to span a wide spectrum of configurations depending on the technology used for protecting a steel plate. The electromagnetic properties of the components in GSP coatings are compiled for the first time in Section II-C.

### A. IRON-ZINC METALLURGY

Galvanization consists in coating a steel plate (or other steel products) with a zinc layer, either by dipping it into a molten-zinc bath (batch and continuous hot-dip galvanization) or by means of electro-plating techniques [11]–[13]. This zinc layer acts as a mechanical and galvanic barrier between the background steel and oxygen, thus preventing corrosion. Batch galvanization is applied to structures that will not require any further mechanical processing (welding, bending, stamping, etc.), while continuous galvanization is applied

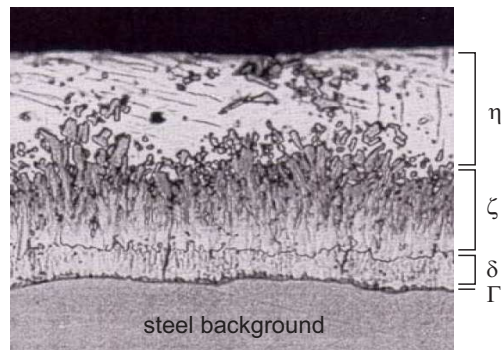


FIGURE 1: A typical micrograph of a galvanic protection coating (courtesy of the American Galvanizers Association, reproduced from [13]), showing the four intermetallic layers that constitute it.

to long steel strips that may be further processed after galvanization, thus requiring a coating ductile enough to withstand intense mechanical deformation. Electroplating is mostly applied when the coating requires a finish with high visual quality [14] and will no further be discussed, being physically equivalent to a pure zinc coating. GSP are typically produced using a continuous coating process, which also allows a more controlled coating thickness, as well as a more precise temperature and exposure time in the zinc bath.

Although hot-dip galvanization uses practically pure zinc, upon interacting with the steel surface a number of complex reactions take place [11], [12], [15], [16], resulting in the appearance of FeZn intermetallic compounds, organized into regular lattices as alloys. Four major FeZn compounds are typically observed, as shown in Fig. 1:  $\eta$  which is predominantly pure zinc;  $\zeta$  with a 5.2-6.1 iron weight percentage (w%);  $\delta$  with a 7-11.5 w%; and  $\Gamma$ , with the highest iron content, in the range 15.8-27.7 w%. Their electromagnetic characteristics are discussed in Section II-C.

The growth of these compounds essentially depends on the zinc bath temperature and duration of immersion. A  $\zeta$  layer first grows very rapidly, with a  $\Gamma$  layer reaching 1  $\mu\text{m}$  thickness in less than one second [12]. For immersion times in excess of two minutes, the  $\zeta$  layer stops growing, with the  $\delta$  picking up and  $\Gamma$  slowly approaching 2  $\mu\text{m}$ . In practice, most GSP present a 1  $\mu\text{m}$  thick  $\Gamma$  layer [17]. For a 450°C bath temperature the  $\delta$  and  $\zeta$  layers reach a similar thickness after about 300 seconds, with a faster growth of the  $\delta$  layer when moving closer to 500°C [12], eventually taking up the entire coating for longer exposure times [15], which are not typically applied in continuous galvanization processes, where times as short as 2 s can be used [18]. While the growth of the  $\zeta$  and  $\delta$  layers are set by the zinc bath temperature and duration [12], [17], the thickness of the  $\eta$  layer is separately controlled at the exit of the bath, by removing the excess liquid zinc from the steel strip, e.g., by means of air blades. It is thus possible to grow coatings in

excess of 100  $\mu\text{m}$ , with a significant content of intermetallic compounds.

In continuous galvanization small amounts (around 0.15%) of aluminum may be added to the zinc bath in order to inhibit iron diffusion, blocking the formation of the brittle  $\zeta$  layer, whose poor mechanical formability would not be compatible with subsequent mechanical processing. This results in considerably thinner coatings, typically between 7 and 20  $\mu\text{m}$  thick but potentially less than 3  $\mu\text{m}$  thick for indoor applications [13], presenting only a  $\eta$  layer [19]. Section II-B discusses how intermetallic compounds can still be grown from these  $\eta$ -only galvanized steel strips through a further thermal treatment.

It should be mentioned that alternative coatings are available, based on higher aluminum content, resulting in a lower corrosion rate compared to pure zinc [12] and better resistance to high-temperature conditions [20], [21]. Given that their share of the market is still small [22], they will not be discussed in the rest of this paper.

This short summary illustrates the considerable diversity in GSP coatings as the underlying cause of the variability of surface conductivity observed in the literature. Ref. [23] stresses that these processes cannot be precisely controlled, and that the thickness of each layer is highly variable and further depends on the presence of trace impurities in the zinc bath and the substrate steel plate [15]. These processes are also affected by cooling conditions after galvanization [16]. In practice the structure of GSP can only be known by means of advanced microscopy analyses and is otherwise only approximately predictable.

## B. GALVANNEALED COATINGS

A special class of GSP of practical importance is produced by applying a heat treatment cycle at the end of a continuous galvanizing line, with the coating having reached its final thickness and only presenting pure zinc. After being reheated around 500°C, zinc in the coating alloys with iron from the steel background. The  $\zeta$  compound first appears, subsequently converted into  $\delta$ . The goal is to minimize the fraction of brittle  $\zeta$ , which has poor formability, instead promoting the more ductile  $\delta$  [12], [24].

This galvanized steel, as it is known, has a lower corrosion rate, since the  $\delta$  compound is less reactive than zinc [25], thus requiring thinner coatings for the same service life. It also features better resistance to scratching and adherence to paint, making it particularly suitable for indoor and automotive applications [24]. Furthermore, the higher resistivity of the  $\delta$  compound (cf. Section II-C) enables more efficient spot-welding, generating more local heat [26], [27]. This major difference in the nature of the surface layer will be shown in Sections III-C and IV to be one of the reasons for the poor surface conductivity observed in certain GSP.

Galvanized GSP can be easily recognized by their low-lustre matte dull appearance, compared to the sheen and typically spangled surface of non-annealed coatings. Yet, galvanizing also results in highly variable coating

structures, typically categorized into three classes: type 0, or under-annealed, where a fraction of pure zinc is still present and  $\zeta$  and  $\delta$  compounds co-exist; type 1, or fully annealed, with no pure zinc left, requires a  $\Gamma$  layer (brittle) at most 1  $\mu\text{m}$  thick and a majority of  $\delta$  compound [21]; and type 2, or over-annealed, sees the  $\Gamma$  layer overgrown potentially up to 2  $\mu\text{m}$  [28]. Accurate chemical analyses of the structure of galvanized coating have confirmed their considerable variability [29], [30].

## C. ELECTROMAGNETIC PROPERTIES

The FeZn compounds created during galvanization processes present very different physical features, caused by their respective lattice structures. In order to understand the reasons for the poor surface conductivity reported for certain GSP, it is fundamental to know their bulk electric conductivity and magnetic permeability.

Zinc, the major contributor to all compounds, is a good conductor at 16.7 MS/m. Yet, lattice perturbations from the inclusion of iron atoms drastically alter its electrical conductivity [31]. Results reported in [32] for several binary metal alloys show reductions mostly exceeding a factor 25 with respect to the respective pure metals. The bulk conductivity of the  $\zeta$  compound was estimated to be 3.3 MS/m in [33], even though it is made up of about 95 w% zinc. The characteristics of the  $\delta$  compound were only investigated a few years ago [34], proving a conductivity at 0.33 MS/m, i.e., a ten-fold loss of conductivity for an iron fraction about twice that of  $\zeta$ .

To the best of our knowledge, no estimate of the conductivity of  $\Gamma$  has been published, but it can be expected to hit a minimum, since results in [32] for binary alloys show that the worst-case scenario is met as soon as the fraction of one of either metals gets close to 30 w%. A rough estimate can be computed by using data for alloys with a similar lattice and electronic structure. It is stated in [35] that the rhodium-zinc compound  $\text{RhZn}_{13}$  is closely related to  $\text{FeZn}_{13}$ , i.e.,  $\zeta$ . The former has a conductivity 2.4 times lower than pure zinc and 3.1 times lower than pure rhodium. For  $\zeta$  the reduction is 5.0 compared to pure zinc and 3.0 compared to pure iron, hence about 50% higher than  $\text{RhZn}_{13}$ . Similarly, the compound  $\text{Rh}_2\text{Zn}_{11}$  has a structure close to  $\text{Fe}_3\text{Zn}_{10}$ , i.e.,  $\Gamma$ . In this case [35] reports a surprising reduction of conductivity by a factor 743 compared to zinc and 965 compared to rhodium. Based on these results, the FeZn compound  $\Gamma$  can be expected to present a worst-case conductivity of the order of 7 kS/m. This value should be regarded as an educated guess: for this reason, the results presented in Section III-C consider two different values for the conductivity of  $\Gamma$ , equal to 7 and 70 kS/m, in order to assess the impact of this imprecise estimate. It will be shown that it has a marginal impact on the apparent conductivity of GSP and that the most important aspect is that  $\Gamma$  is expected to present a significantly lower conductivity than  $\delta$ .

Moving to relative magnetic permeability, pure iron exceeds  $10^4$  at DC [36]. Although being predominantly

	units	Intermetallic ZnFe compounds			
		$\eta$	$\zeta$	$\delta$	$\Gamma$
Fe	w%	< 0.03	5.2-6.1	7-11.5	15.8-27.7
$\mu_i - 1$	-	$-10^{-11}$	$10^{-5}$	$10^{-6}$	$\ll 1$
$\sigma_i$	MS/m	16.7	3.3	0.33	0.007   0.07
$\delta_i$ (1 GHz)	$\mu\text{m}$	3.89	8.76	27.7	190   60.1
$\Gamma'_i$	-	-	0.385	0.519	0.746   0.369

TABLE 1: Physical characteristics of ZnFe intermetallic compounds found in galvanizing coatings: iron weight percentage, magnetic susceptibility  $\mu_i - 1$  (order of magnitude only reported), DC electric conductivity, skin depth at 1 GHz and surge reflectivity between adjacent layers (cf. III-C). Two estimates for the conductivity of the  $\Gamma$  compound and related quantities are shown.

made of iron, steels are complex multi-element alloys, with carbon as the main addition. The presence of impurities not only affects an alloy conductivity, but more drastically impact its magnetic permeability [31], [36]. The  $\zeta$  compound was shown in [37], [38] to be weakly paramagnetic, a result confirmed and refined in [33]. A similar conclusion was drawn for the  $\delta$  compound in [34], while previous results cited in [33] pointing to  $\Gamma$  as also being paramagnetic, although no precise value is available for its magnetic susceptibility. All these results are summarized in Table 1, and allow to conclude that only steel has a significant magnetic behavior in GSP, as discussed in Section III-A.

### III. APPARENT CONDUCTIVITY OF STEEL PLATES

The surprisingly low conductivity reported in [4] for bare steel plates were tentatively explained in terms of their surface roughness being far larger than their skin depth. The same reason was suggested for galvanized and zinc-plated steels. In fact, recent results have proven that surface roughness cannot explain a more than 20-fold conductivity reduction: measurements up to 360 GHz were shown in [39] to result in less than 20% reduction compared to DC conductivity for silver samples; similar results are reported in [40] and [41] for the THz range, where the skin depth is also negligible compared to surface roughness; results in [42] for stainless steel up to 2 THz also show no major impact of surface roughness. A higher reduction of about 50% was reported in [43], but dealt with sub-micrometer thin films, thinner than the skin depth.

This section provides an alternative explanation, introducing first-principle based models, first discussing the microwave behavior of bulk steel (Section III-A) and how its effective conductivity is modified by a metal coating (Section III-B), resulting in a characteristic dispersive response. A multi-layer model based on the physical structure of GSP (cf. Section II) is presented in Section III-C, leading to the prediction that the conductivity of a GSP strongly depends on the galvanizing technology and does not necessarily result in a poor conductivity.

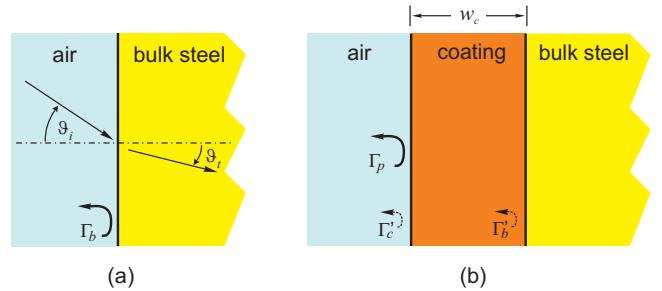


FIGURE 2: Wave interacting with: (a) bulk steel and (b) single-layer coated steel. Primed quantities represent surge reflection coefficients (cf. Section III-B).

#### A. BARE STEEL PLATES

The case of a half-space bulk metal of conductivity  $\sigma_b$  and relative permeability  $\mu_b$  will be first considered, as depicted in Fig. 2(a). A plane wave impinging along an angle  $\theta_i$  would generate a non-homogeneous plane wave across the metal interface. Given that the refractive index of a conductor is complex, Snell law cannot be used for computing the outgoing direction  $\theta_t$  of the transmitted wave. Instead, enforcing the continuity of the tangential components of the two half-space propagation constants over the interface between them requires that,

$$\sin \theta_t = \sqrt{\frac{2\omega\epsilon_0}{\mu_b\sigma_b}} \sin \theta_i. \quad (1)$$

For microwave applications  $\sigma_b\mu_b \gg \omega\epsilon_0$ , hence  $\sin \theta_t \simeq 0$  and the transmitted wave will be approximated as propagating perpendicular to the interface. The reflectivity of the metal surface can be expressed as [44]

$$\Gamma_b = \frac{\cos \theta_i - \sqrt{\sigma_b/j\omega\epsilon_0\mu_b}}{\cos \theta_i + \sqrt{\sigma_b/j\omega\epsilon_0\mu_b}} \quad (2)$$

for a TE incidence; the TM case will not be discussed, since it leads to the same conclusions. This expression can be further simplified into

$$\Gamma_b = -1 + 2 \cos \theta_i \sqrt{j\omega\epsilon_0\mu_b/\sigma_b} \quad (3)$$

after the more stringent condition

$$\sqrt{\sigma_b/\omega\epsilon_0\mu_b} \gg 1 \quad (4)$$

which is met even by conductors with  $\sigma_b < 1$  MS/m well into the THz range, where (3) is also known as Hagen-Rubens relation [45]. Approximation (3) shows that the reflectivity from the metal interface depends on the quantity

$$\sigma'_b = \sigma_b/\mu_b \quad (5)$$

which acts as its *effective bulk conductivity*.

It is important to understand if  $\sigma'_b$  is frequency dependent (dispersive). The conductivity of metals, as modeled by means of Drude model, is expected to be fundamentally constant over frequencies well above the THz range, with the metal response changing only when approaching infrared

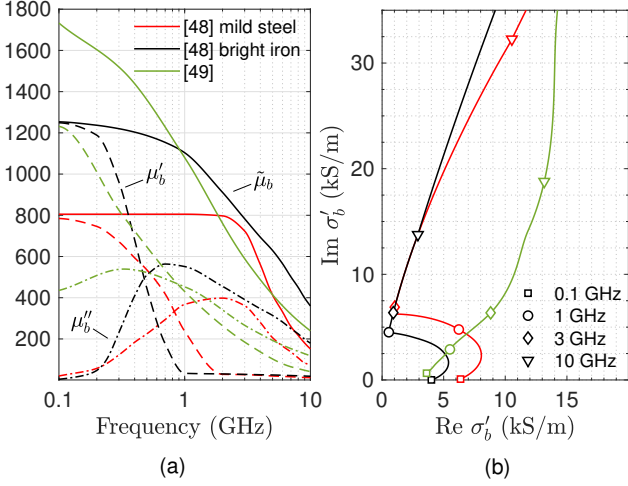


FIGURE 3: Bulk steel: (a) complex permeability  $\mu_b = \mu'_b - j\mu''_b$  and effective dissipative permeability  $\tilde{\mu}_b$ , defined in (7); (b) effective bulk conductivity  $\sigma'_b$ , based on a conductivity  $\sigma_b = 6$  MS/m. Results processed from steel magnetic permeability data reported in the references in the legend.

frequencies [42]. Hence,  $\sigma_b$  will be set to steel DC conductivity, typically 4-8 MS/m in mild carbon steels, decreasing to 1-3 MS/m for stainless steels [36], [46], [47]. On the other hand, steels present a highly dispersive and complex relative permeability [48], [49]. Contrary to a widespread belief, stainless steels are ferromagnetic too, apart those with austenitic structure [46].

Fig. 3(a) shows the complex relative permeability  $\mu_b = \mu'_b - j\mu''_b$  of three data sets from [48], [49], representing typical results for structural steels. They share similar features, with  $\mu'_b > \mu''_b$  around 0.1 GHz and  $\mu'_b < \mu''_b$  above 1-3 GHz;  $\mu'_b$  and  $\mu''_b$  are still significantly larger than one at 10 GHz. These features directly affect the effective bulk conductivity  $\sigma'_b$ . Fig. 3(b) shows the complex  $\sigma'_b$  obtained from (5), for  $\sigma_b = 6$  MS/m, featuring a prominent imaginary part above 1 GHz. Both real and imaginary parts are smaller than 30 kS/m below 10 GHz, more than two orders of magnitude lower than the 6 MS/m DC conductivity, a reduction due to the non-negligible steel permeability.

Given that  $\sigma'_b$  is complex, it is not immediately clear how it is related to power dissipation by a steel surface. Most experimental methods for measuring the conductivity of metals rely on power dissipation phenomena, e.g., in resonance cavities or waveguides [4], [41], [50], [51]. For this reason we suggest an alternative definition of the effective conductivity, based on the loss factor  $1 - |\Gamma_b|^2$ , with  $\Gamma_b$  given in (3). As proven in Appendix A

$$1 - |\Gamma_b|^2 \simeq 4 \cos \theta_i \sqrt{\frac{\omega \epsilon_0 \tilde{\mu}_b}{2\sigma_b}} \quad (6)$$

where

$$\tilde{\mu}_b = d(\mu_b) = |\mu_b| - \text{Im} \mu_b = |\mu_b| + \mu''_b \quad (7)$$

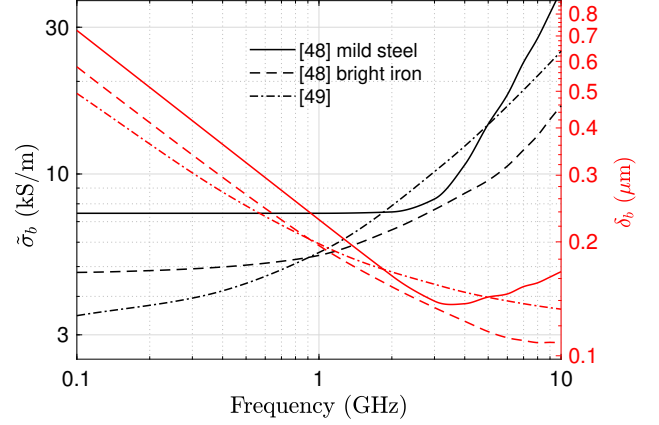


FIGURE 4: Power dissipation in bulk steel: effective dissipative conductivity  $\tilde{\sigma}_b$  and skin depth  $\delta_b$  versus frequency, for a DC conductivity  $\sigma_b = 6$  MS/m.

is the *effective dissipative permeability*, modeling how the complex nature of the permeability  $\mu_b$  affects the power dissipation. Fig. 3(a) shows how  $\tilde{\mu}_b$  evolves smoothly with the frequency, monotonously decreasing above 1 GHz, though not vanishing.

Comparing (6) to (5) dissipation losses can be explained in terms of the *effective dissipative conductivity*  $\tilde{\sigma}_b$

$$1/\tilde{\sigma}_b = d(1/\sigma'_b) = \tilde{\mu}_b/\sigma_b, \quad (8)$$

where the last result holds only for a real  $\sigma_b$ . Appendix A shows that (7) must also be applied when computing steel skin depth.

Fig. 4 shows  $\tilde{\sigma}_b$  increasing monotonously with the frequency, as the magnetic dissipative permeability decreases; the three curves available share very similar traits, even though their absolute values differ noticeably. The frequency dependence is opposite that expected from surface roughness, since the conductivity increases with the frequency. Even so,  $\tilde{\sigma}_b$  is lower than 40 kS/m. Results in [4] found 100 kS/m at 8.42 GHz, while results from Vane reported in [52] found 36 kS/m at 3.0 GHz. Although these results already display a significant dispersion, it will be shown in Section III-B to significantly differ from results expected for GSP, as confirmed from empirical results in Section IV-C.

Since steel plates are typically at least 1 mm thick, i.e., much thicker than the skin depth shown in Fig. 4, steel plates will be approximated as half-space regions in the rest of the paper. Kittel's permeability data [49] will be taken as a more general reference, since based on regression curves obtained from multiple previous literature results.

## B. SINGLE-LAYER COATING

As recalled in Section II, steel plates typically require galvanic protection against corrosion. Before dealing with multilayered coating structures (cf. Section III-C), it is important to understand how the presence of a metallic coating layer alters the apparent conductivity of steel plates.

Fig. 2(b) shows the configuration of interest, with a homogeneous coating layer of thickness  $w_c$  and conductivity  $\sigma_c$  interposed between the background steel, with effective bulk conductivity  $\sigma'_b$ , and the air interface. Following the review of the properties of zinc-based coatings in Section II-C, it will be assumed to have a relative magnetic permeability  $\mu_c = 1$ .

The overall reflectivity  $\Gamma_p$  at the plate surface can be derived as a function of surge reflectivities (indicated as primed quantities in Fig. 2(b)) at each interface, i.e., the reflectivity associated to the case where each material occupy a half-space region. As shown in Section III-A after crossing an air-metal interface a wave propagates along  $\theta_t \simeq 0$ , thus impinging normally onto the background steel interface. In this case the surge reflectivity  $\Gamma'_b$  at the internal coating-steel interface reads

$$\Gamma'_b = \frac{1 - \sqrt{\sigma'_b/\sigma_c}}{1 + \sqrt{\sigma'_b/\sigma_c}}, \quad (9)$$

while the air-coating surge reflectivity  $\Gamma'_c$  is found from (3). The plate reflectivity  $\Gamma_p$  is the result of multiple internal reflections over the two interfaces and is readily found from the surge reflectivities as [53, Section 4.4.4]

$$\Gamma_p = \frac{\Gamma'_c + \exp(-j2k_c w_c)\Gamma'_b}{1 + \Gamma'_c\Gamma'_b \exp(-j2k_c w_c)} \quad (10)$$

where  $k_c = (1 - j)/\delta_c$  and  $\delta_c = 1/\sqrt{\pi\nu\mu_0\sigma_c}$  is the skin depth in the coating layer. The same approximation applied in the derivation of (3) can now be applied to (10), since condition (4) still holds. As a result

$$\begin{aligned} \Gamma_p &= -1 + 2 \cos \theta_i \sqrt{j\omega\epsilon_0/\sigma_c} \frac{1 + \exp(-j2k_c w_c)\Gamma'_b}{1 - \exp(-j2k_c w_c)\Gamma'_b} \\ &= -1 + 2 \cos \theta_i \sqrt{j\omega\epsilon_0/\sigma_c} \frac{1 + \sqrt{\sigma'_b/\sigma_c} \tanh(jk_c w_c)}{\sqrt{\sigma'_b/\sigma_c} + \tanh(jk_c w_c)} \end{aligned} \quad (11)$$

Comparing (11) to (3) it is now possible to define the *apparent bulk conductivity* of a single-layer coated plate as

$$\sigma_a = \sigma_c \left( \frac{\sqrt{\sigma'_b/\sigma_c} + \tanh(jk_c w_c)}{1 + \sqrt{\sigma'_b/\sigma_c} \tanh(jk_c w_c)} \right)^2. \quad (12)$$

Fig. 5(a) shows  $\sigma_a$  versus frequency for a coating conductivity  $\sigma_c$  equal to 0.3, 3 and 15 MS/m. These values loosely approximate those expected for the intermetallic compounds making up zinc-based coatings. The thickness  $w_c$  associated to each of these single-layer coatings is equal to 50, 5 and 1  $\mu\text{m}$ , respectively. The rationale behind these choices will become apparent at the end of this section.

The first important point to notice is how a metallic coating leads to an apparent plate conductivity deeply different from the effective conductivity of bare steel<sup>1</sup>, shown in Fig. 3(b). The three coatings share a similar trajectory across the complex plane, with  $\sigma_a$  converging to  $\sigma_c$  as the frequency

<sup>1</sup>based on  $\sigma_b = 6$  MS/m and Kittel's permeability data, as discussed at the end of Section III-A

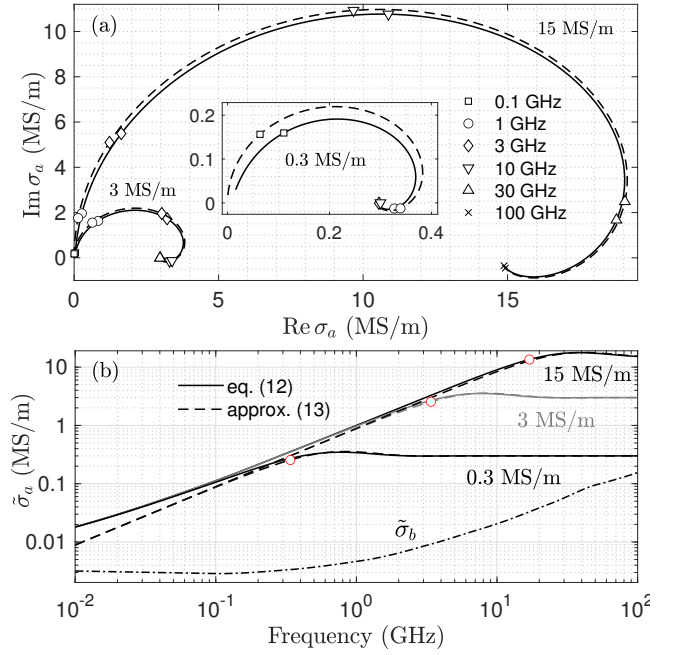


FIGURE 5: Single-layer coating: (a) apparent conductivity  $\sigma_a$  and (b) dissipative apparent conductivity  $\tilde{\sigma}_a$ . Three values of  $\sigma_c$  are considered, all sharing the same product  $w_c\sigma_c = 15$  S. Solid lines obtained using Kittel's steel permeability data, dashed lines assuming a high contrast between coating and steel effective conductivities. The dash-point line shows the effective dissipation  $\tilde{\sigma}_b$  of bare steel, based on Kittel's data (Section III-A). Red circles in (b) stand for the frequency at which  $w_c = \delta_c$ , marking the end of the transition region.

increases enough for  $w_c > \delta_c$ . At this point any impinging wave would mostly interact with the coating, reaching the steel background significantly attenuated.

For the three examples in Fig. 5  $\sigma_c \gg \sigma'_b$ , i.e., a high contrast between steel and coating effective conductivities. In this case (12) simplifies into

$$\sigma_a \simeq \sigma_c \tanh^2(jk_c w_c). \quad (13)$$

This approximation is shown in Fig. 5 as dashed lines, proving that it accurately predicts the frequency evolution of the apparent plate conductivity, apart at very low frequency. Hence, it is not necessary to have a precise knowledge of  $\sigma'_b$ , as long as it is negligible compared to  $\sigma_c$ .

The power dissipation by a coated plate can be found as for bare steel, by using the apparent conductivity  $\sigma_a$  instead of  $\sigma'_b$  in (6) and (8), yielding the *apparent dissipative conductivity*

$$1/\tilde{\sigma}_a = d(1/\sigma_a) \quad (14)$$

of the coated plate, shown in Fig. 5(b). For frequencies such that  $w_c < \delta_c$  (on the left of the red circles),  $\tilde{\sigma}_a$  undergoes a transition between  $\sigma_c$  (high-frequency limit) and  $\tilde{\sigma}_b$  (low-frequency limit).

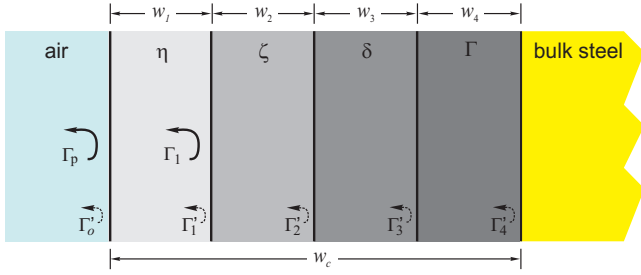


FIGURE 6: Multi-layer coating model, divided into the four main FeZn intermetallic compounds created during typical galvanization processes. Primed quantities stand for surge reflectivities at each interface.

An asymptotic approximation of (12), in the limit of a high contrast  $\sigma_c \gg \sigma'_b$  and  $w_c < \delta_c$ , shows that in this transition region  $\tilde{\sigma}_a$  scales linearly with the frequency

$$\tilde{\sigma}_a \simeq \pi\nu\mu_0(w_c\sigma_c)^2. \quad (15)$$

Therefore, coated steel plates sharing the same  $w_c\sigma_c$  product would dissipate the same amount of power, with differences in the coating conductivity  $\sigma_c$  becoming apparent only at frequencies such that  $w_c > \delta_c$ . Below this frequency,  $\tilde{\sigma}_a$  can span several orders of magnitude, covering a wider range than expected for bare steel (cf. Fig. 4). Because in the transition region  $\tilde{\sigma}_a \sim (w_c\delta_c)^2$ , it is highly sensitive to variations in the coating thickness or conductivity.

These results help understand why even electro-plated steel plates, where  $\sigma_c = 16.7$  MS/m, can present significant dissipation, if  $w_c < \delta_c$ . The results in Fig. 5(b) make it clear that below 3 GHz a 1  $\mu\text{m}$  thick highly conductive coating at 15 MS/m (close to pure zinc), would introduce the same loss than a bulk metal with conductivity 3 MS/m.

In conclusion, the very existence of the transition region is a distinctive feature pointing to the presence of a background metal (here steel) with poor effective bulk conductivity, compared to the coating. Confirming this prediction necessarily requires empirical observations of the apparent conductivity over a relatively wide band, as presented in Section IV.

### C. MULTI-LAYERED COATING

As discussed in Section II, GSP typically present multi-layered coatings, whose structure depends on the galvanization technology. This section shows how the single-layer model can be extended to this more complex configuration and how the apparent conductivity is affected.

Fig. 6 shows a four metal-layer model based on the micrograph in Fig. 1. Each layer is characterized by a conductivity  $\sigma_i$  and thickness  $w_i$ , with  $i = 4$  corresponding to the last layer ( $\Gamma$  compound) interfacing with steel. Normal incidence through all internal layers is assumed, as argued in Section III-A. The surge reflectivity  $\Gamma'_i$  at each internal interface ( $i < 4$ ) can be computed as in (9), substituting the contrast ratio  $\sigma_{i+1}/\sigma_i$  under the square root. The bulk DC conductivities are used instead of the effective bulk ones,

#	Layer thickness				Equiv. coating cond. $\sigma_c$ (MS/m)		
	$\eta$	$\zeta$	$\delta$	$\Gamma$	5 $\mu\text{m}$	10 $\mu\text{m}$	20 $\mu\text{m}$
1	100	0	0	0	16.7(16.7)	16.7(16.7)	16.7(16.7)
2	10	90	0	1	3.7(3.7)	4.2(4.2)	4.5(4.5)
3	10	45	45	1	2.7(2.6)	3.0(3.0)	3.3(3.3)
4	0	50	50	1	1.5(1.5)	1.6(1.6)	1.8(1.8)
5	0	10	90	1	0.52(0.50)	0.57(0.56)	0.60(0.60)
6	0	0	100	1	0.28(0.27)	0.30(0.30)	0.32(0.31)
7	0	0	100	2	0.23(0.20)	0.28(0.27)	0.31(0.30)

TABLE 2: Seven coating structures representing typical configurations for GSP. The thickness  $w_4$  of the  $\Gamma$  layer is given in  $\mu\text{m}$ , whereas the remaining layers are expressed as percentage of  $w_c - w_4$ . The equivalent coating conductivity  $\sigma_c$  is shown for each configuration, as defined in Section III-C, for three values of coating thickness  $w_c$ .  $\Gamma$  conductivity set at 70 kS/m and 7 kS/m (in parenthesis).

since none of the ZnFe compounds presents any significant magnetic behavior (cf. Section II-C); clearly, the effective conductivity must be used for the steel background. Table 1 gives the surge reflectivities at each internal interface between two ZnFe compounds: all appear to be non-negligible, implying significant multiple interactions.

The apparent conductivity of the GSP can be computed from (11), by substituting the reflectivity  $\Gamma_1$  at the first inner interface for the bulk steel reflectivity  $\Gamma'_b$ . This yields

$$\sigma_a = \sigma_1 \left( \frac{1 - \exp(-j2k_1w_1)\Gamma_1}{1 + \exp(-j2k_1w_1)\Gamma_1} \right)^2 \quad (16)$$

with the dissipative apparent conductivity given by (14). The reflectivity  $\Gamma_1$  can be found by applying (10) to compute iteratively the reflectivity at the inner interfaces

$$\Gamma_{i-1} = \frac{\Gamma'_{i-1} + \exp(-j2k_iw_i)\Gamma'_i}{1 + \Gamma'_{i-1}\Gamma'_i \exp(-j2k_iw_i)} \quad (17)$$

starting from the interface with bare steel for  $i = 4$ .

This model was applied in order to understand how the apparent conductivity of GSP is affected by their coating structure. Seven different configurations were selected, described in Table 2, covering the main cases found in practical applications (cf. Section II): from a pure-zinc coating (case #1) to an over-annealed one (case #7).

The apparent conductivity for each case is shown in Fig. 7(a), for a coating thickness  $w_c = 10$   $\mu\text{m}$ . These results are broadly similar to those for a single-layer coating in Fig. 5, but apart for a pure-zinc coating (case #1), which has a single layer, all the others present a more complex trajectory over the complex plane. These differences are explained by the fact that as the frequency increases enough to have the thickness of one layer exceeding its skin depth, i.e.,  $w_i > \delta_i$ , a wave would be prevented from interacting with deeper layers. For instance, at low frequency case #3 is heavily affected by the poor conductivity of the  $\delta$  layer, but above 3 GHz a wave would hardly interact with it, resulting in a

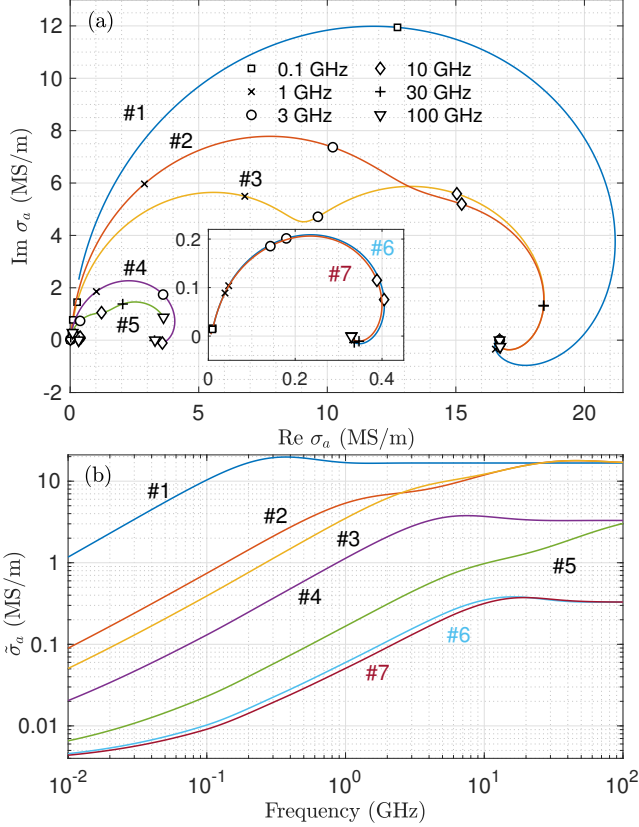


FIGURE 7: Multi-layer coating: (a) apparent conductivity and (b) dissipative apparent conductivity, for the seven coatings structures described in Table 2 and a thickness  $w_c = 10 \mu\text{m}$ .

sudden increase in the apparent conductivity, due to most dissipation now taking place across  $\zeta$  and  $\eta$  layers.

Using (14), the results in Fig. 7(a) are converted into the apparent dissipative conductivity  $\tilde{\sigma}_a$  in Fig. 7(b), where a transition region similar to the single-layer case can be observed for all seven configurations. The convergence to a constant conductivity is reached only once the thickness of the outer layer exceeds its skin depth, i.e., when the outer layer acts as a bulk conductor, effectively shielding inner layers, and background steel, from incoming waves. The skin depths shown in Table 2, evaluated at 1 GHz, imply that the convergence to a constant apparent conductivity strongly varies depending on what ZnFe compound appears at the GSP surface. Two extreme cases in Fig. 7(b) are #1 and #5, where the outer layers are  $\eta$  (pure zinc) and  $\zeta$ , respectively, resulting in #1 converging around 1 GHz whereas #5 is expected to fully converge only above 100 GHz, because of the presence of a very thin outer layer.

Conversely, in the transition region a GSP sees waves propagating across all coating layers, which implies  $w_i < \delta_i, \forall i$ . In this case a multilayer coating behaves as a single homogeneous conductor, with an equivalent coating conductivity  $\sigma_c$  that can be estimated by least-square fitting

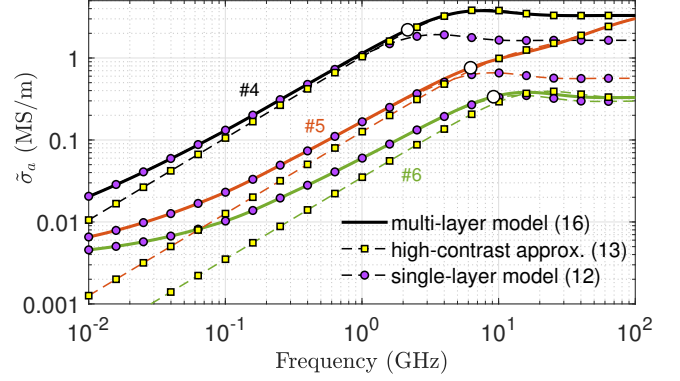


FIGURE 8: Comparison of the multi-layer model (16), using Kittel's steel magnetic data, with two approximate models: i) the single-layer model (12) least-square fitted to the transition region and ii) the multi-layer model assuming infinite steel effective resistivity, or high-contrast approximation (13). Large white circles mark the end of the transition region, defined by the condition that layer thicknesses  $w_i < \delta_i, \forall i$ . All results for a  $10 \mu\text{m}$  coating.

the single-layer model (12) to the results in Fig. 7(b). Fig. 8 shows how this operation accurately reproduces  $\tilde{\sigma}_a$  over the entire transition region of cases #4 to #6. This approach has the advantage of simplifying the comparison of different coating structures, as shown in Section IV-C.

The values of  $\sigma_c$  thus found are shown in Table 2 to weakly depend on the coating thickness  $w_c$ , and are rather controlled by the relative thickness of the four ZnFe compound layer, i.e., the coating technology. It can also be observed how  $\sigma_c$  is practically unaffected by assuming a  $\Gamma$  conductivity equal to 7 or 70 kS/m. This result is explained by the fact that the skin depth for  $\Gamma$  (cf. Table 1) is much larger than its typical 1-2  $\mu\text{m}$  thickness; as such, dissipation is negligible, making  $\Gamma$  effectively transparent.

Fig. 8 also shows the results obtained by assuming a negligible steel conductivity, equivalent to the high-contrast approximation (13). For cases #5 and #6, involving only  $\delta$  and  $\Gamma$  compounds, this approximation is no longer accurate, since the contrast between their conductivity and steel is no longer very high. Therefore, it is necessary to model the steel background as discussed in Section III-A.

These results help understanding why widely different values of the apparent conductivity of GSP have been reported [4], depending on the coating technology. The prediction of a transition region as a common feature in GSP also exacerbates this variability, as confirmed by the results presented in Section IV-C. It can be concluded that it would be overly optimistic to expect that galvanization always improves the apparent conductivity of steel plates, unless the thickness and coating technology are selected carefully. As an example, Fig. 7(b) shows a thousand-fold increase in conductivity when passing from #7 to #1 at 100 MHz, even though  $\sigma_c$  only increases by a factor sixty,

confirming that GSP losses can be very effectively reduced without necessarily opting for thicker coatings, as predicted by (15).

#### IV. WIDE-BAND CONDUCTIVITY ESTIMATES FROM POWER LOSS IN REVERBERATION CHAMBERS

The models introduced in Section III predict that the apparent dissipative conductivity  $\tilde{\sigma}_a$  of GSP are expected to be highly variable because of: i) a transition region where  $\tilde{\sigma}_a$  approximatively scales linearly with the frequency, and ii) high variability of the coating equivalent conductivity  $\sigma_c$ , depending on the coating technology. This last point was already empirically observed in [4], but apparent conductivities were only estimated at 8.42 GHz, since resonator-based characterization techniques were used [4], [41], [51], as they are better suited to the characterization of good conductors [54], [55]. Wide-band techniques such as those based on transmission and reflection through waveguides [56], commonly used for dielectric materials, are not suitable for conductors, since their reflectivity is weakly sensitive to the metal conductivity, as clear from (3). As a result, the existence of the transition region has not been demonstrated to be a common feature of GSP, to the best of our knowledge.

Instead of relying on single-mode microwave resonators, we exploited wide-band experimental results of insertion losses observed in reverberation chambers (RC). These test facilities are sealed metal boxes with dimensions much larger than the wavelength at which they are operated, in order to present multiple overlapping resonances [57]–[59]. Thanks to the high reflectivity of their metal walls and surfaces, they generate random field distributions statistically covering all directions of arrival with the same probability [58], [60]. This property is exploited in evaluating the radiation immunity and the power radiated by electronic devices over multi-decade bandwidths. International standards such as [61] require that an RC be fully characterized before being operated as a test facility, thus offering the opportunity to precisely know how much power is lost on its metal walls and surfaces.

Since most RC are made of GSP, they offer an ideal opportunity for testing theoretical predictions from the previous section. The existence of a large literature dealing with RC offers the opportunity to assess differences across these implementations: not only because each RC may be built with GSP based on different coating technologies, but also because their dimensions span a very wide range, thus extending the frequency range over which power-loss results are available, as shown in Section IV-C.

To this end, we first discuss in Section IV-A how  $\tilde{\sigma}_a$  can be estimated from insertion losses in an RC. The criteria applied in selecting data published in the RC literature are explained in Section IV-B, while Section IV-C summarizes the main findings of this analysis.

##### A. REVERBERATION CHAMBER THEORY

The main figure of merit of an RC is its composite quality factor  $Q$ , defined on the basis of the average energy stored

by its overlapping resonant modes [57], [62]. Given an RC of volume  $V$ , its  $Q$  is limited by power-dissipation phenomena, mostly by interaction with its inner metal surfaces covering an area  $S$ , leakage through antennas and absorption in lossy dielectric materials, e.g., foam absorbers. It is possible to break down the composite quality factor into  $N$  partial contributions  $Q_n$  for each of these phenomena, as [62]

$$Q^{-1} = \sum_{n=1}^N Q_n^{-1}. \quad (18)$$

The power leaked by an ideal antenna can be modeled by means of the partial quality factor [62]

$$Q_a^\circ = 16\pi V/\lambda^3 \quad (19)$$

with  $\lambda$  the wavelength. In practice, for  $N_a$  identical antennas with a radiation efficiency  $\eta_a$  and input reflection coefficient  $\Gamma_a$ , the partial quality factor becomes [63]

$$Q_a = Q_a^\circ / (N_a + 1)(1 - \eta_a^2 |\Gamma_a|^2) \quad (20)$$

with the plus one due to enhanced backscattering at the transmitting antenna [64]. Typically test setups involve a set of two identical antennas.

Dissipation on an RC metal surfaces is modeled as [9]

$$Q_w = \frac{3V}{2S} \sqrt{\pi\mu_0\nu\tilde{\sigma}_a} \quad (21)$$

taking into account the apparent dissipative conductivity of metal plates. It is therefore possible to estimate  $\tilde{\sigma}_a$  from  $Q_w$ ,

$$\tilde{\sigma}_a = 4S^2 Q_w^2 / 9V^2 \pi\mu_0\nu, \quad (22)$$

while  $Q_w$  is estimated from the composite quality factor  $Q$

$$Q_w^{-1} = Q^{-1} - Q_a^{-1}. \quad (23)$$

Appendix B discusses the conditions required for this last operation to be accurate.

##### B. SELECTION CRITERIA FOR LITERATURE DATA

RC are widely used as test facilities for antenna characterization, over-the-air tests in wireless communications and electromagnetic compatibility tests. As such, more than 200 papers were considered as sources of experimental results from which the apparent conductivity of GSP could be estimated. In practice, only a fraction of these are reported in Section IV-C, based on several requirements. First, a detailed description of the test setup, confirming that GSP were used, including the number of antennas and their characteristics, cavity dimensions, etc. Second, the absence of any potential source of additional losses that would make it difficult to estimate the fraction of power dissipated by metal surfaces; e.g., wooden supports often used as antenna stands [65], foam absorbers widely used in over-the-air tests [66] or any removable opening/joint in the cavity hull. Third, results should span a multi-octave bandwidth, in order to provide evidence of the transition region; this excludes results from millimeter-wave tests and wireless device tests, since they are

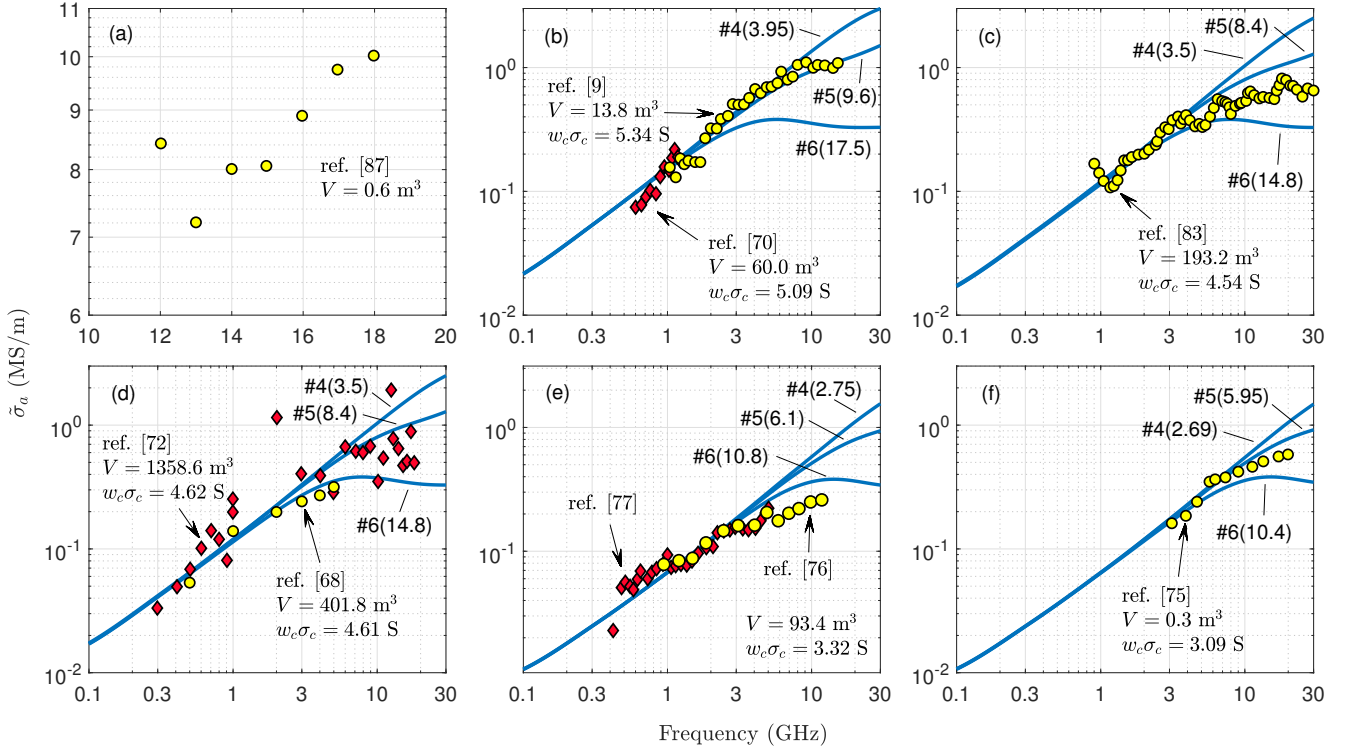


FIGURE 9: Apparent dissipative conductivity estimated from RC literature data: (a) aluminum-alloy cavity with 8.86 MS/m conductivity, (b)-(f) GSP based cavities. References from which the data were extracted are shown in each figure, together with the volume of the RC and the product  $w_c \sigma_c$  of their GSP estimated from the transition region. Solid lines are theoretical results based on the multi-layer model described in Section III-C, for some of the coating structures described in Table 2, for the thickness indicated in parenthesis (micrometers).

narrow-band. References [9], [67]–[85] meet these criteria and provide the basis for the analysis in Section IV-C.

Even with these precautions, it is still necessary to consider the uncertainty associated to these results. An uncertainty budget is discussed in Appendix B, and requires knowledge of the number of data samples from which the quality factor  $Q$  was estimated. Unfortunately, this information is not systematically provided, making it impossible to establish the uncertainty of each data set. Still, it is possible to consider that in the worst case the expanded uncertainty is limited to about  $\pm 40\%$  in case  $Q$  at each frequency is based on a minimum 100 independent samples, with many data sets often based on a significantly higher number of samples.

It is worth stressing that the aim sought here is to obtain experimental evidence of the existence of the transition region and of a strongly reduced apparent conductivity in the lower-frequency range, due to the constraints created by the multi-layer structure of protective zinc-based coatings, rather than to introduce a novel method to accurately estimate the conductivity. As such, this level of uncertainty can be deemed sufficient, because significantly smaller than the change in the apparent conductivity observed in the results presented in Section IV-C.

### C. RESULTS

The proposed method was first applied to data measured in an aluminum-alloy cavity [86], whose conductivity was separately tested to be 8.86 MS/m. The conductivity estimated from the cavity  $Q$  factor using (22), after taking into account the presence of an aperture, is shown in Fig. 9(a). The results are in good agreement with the reference conductivity, confirming the accuracy of the proposed method, within the uncertainty proper to RC, as discussed in Appendix B.

Results in Figs. 9(b)-(f) were instead obtained from data measured in cavities build from GSP; references for each data set are provided in each figure. All these results feature a transition region, where  $\tilde{\sigma}_a$  broadly scales linearly with the frequency, consistent with the predictions of Section III-C. As argued there, the response in the transition region only depends on the product  $w_c \sigma_c$ . This product was estimated by least-square fitting the single-layer model (12) to the transition region of each data set. The values of  $w_c \sigma_c$  thus obtained are shown in each figure, and range from 3 to 5 S.

Instead, at higher frequencies the conductivity grows more slowly, which was shown in Section III-C to occur when the skin depth of the outer layer becomes comparable to its thickness. The frequency at which this change of rate is observed was shown in Section III-C to be intimately related

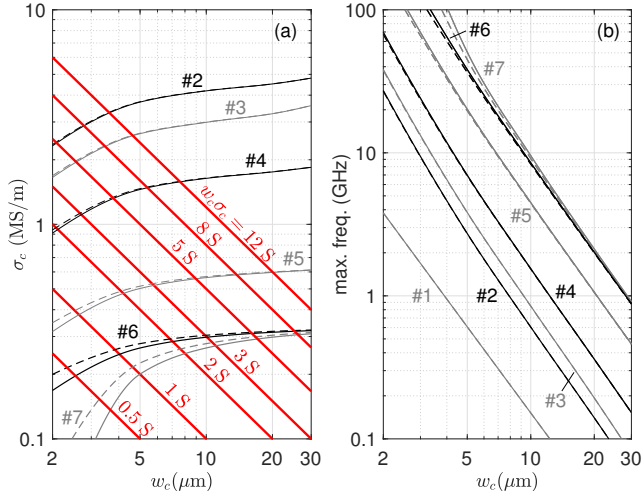


FIGURE 10: Equivalent single-layer modelling of multi-layered coatings: (a) equivalent conductivity  $\sigma_c$  versus coating thickness, for structures #2 to #7 described in Table 2, for a  $\Gamma$  layer conductivity equal to 7 kS/m (solid curves) and 70 kS/m (dashed curves); red lines show the loci of constant  $w_c\sigma_c$  products. (b) maximum frequency for the transient region versus coating thickness.

to the coating technology.

It is therefore possible to assess what technologies are more likely to explain each data set. This can be done thanks to Fig. 10(a), which extends the results in Table 2, presenting the effective coating conductivity  $\sigma_c$  as a function of its thickness  $w_c$ , for the six coating structures from #2 to #7. The thickness  $w_c$  required for each candidate coating structure is found at the intersection with the red line, corresponding to the value of  $w_c\sigma_c$  estimated from the transition region of each data set, and the  $\sigma_c$  curve expected for each coating structure. It was argued in Section III-B that as  $w_c$  increases, the maximum frequency of the transition region is expected to decrease. This inverse relationship is shown in Fig. 10(b), helping to assess what coating structures are compatible with each data set.

Having estimated the coating thickness  $w_c$  for each candidate coating structure, the entire frequency evolution of the apparent conductivity can be computed using the multi-layer model described in Section III-C. These theoretical results are shown as solid lines in Figs. 9(b-f) and by definition overlap at low frequencies, since they all share the same  $w_c\sigma_c$  value. Only a selected group of coating structures are presented, corresponding to those providing a closer agreement with empirical results, which requires matching the end of the transition region. Fig. 9(b) clearly shows that only coating #5 is consistent with the results, for a 9.6  $\mu\text{m}$  thickness. A 3.95  $\mu\text{m}$  thick coating #4 has a transition region extending beyond the data, as would also be the case for #3 and #2 from Fig. 10. On the other hand, coating #6 would converge at a lower frequency. Case #7 can be seen in Fig. 10(a) to significantly differ from #6 only

for  $w_c\sigma_c < 2$  S.

Similar results are found for the rest of Fig. 9, with mostly coatings #5 and #6 displaying the best agreement; estimated values of  $w_c$  shown for each curve range between 5 and 11  $\mu\text{m}$ , thus pointing to galvanized GSP. This hypothesis makes sense, since RC are indoor facilities, thus suitable for this coating technology, as also confirmed by the matte aspect observed in published RC pictures. It is worth noting the remarkable self-consistency of these results, which were obtained from data measured in RC of very different dimensions, ranging from 0.3 to 1359 cubic meters.

Further results are presented in Fig. 11, sorted for  $w_c\sigma_c$  decreasing from 4.21 S to 0.41 S. No significant deviation from the transition region is observed now, suggesting that these GSP must have an either thin or poorly conductive coating, as implied by Fig. 10(b). It is nonetheless still possible to restrict the number of possible coating technologies explaining these results, based on the estimated coating thickness. Fig. 11(a) shows that #6 (and therefore #7, too) would deviate from the transition, while #3 (as well as #2) would require  $w_c < 2$   $\mu\text{m}$ , which is unlikely, thus pointing again at a galvanized coating. Similar observations are found for Figs. 11(b)-(d). Figs. 11(e)-(i) present data where either the maximum frequency or  $w_c\sigma_c$  are too low to distinguish between different coating technologies, apart by excluding #1 to #4 since requiring exceedingly thin coatings. Model results for #6 and #7 yield consistent estimates of  $w_c > 3$   $\mu\text{m}$ , in agreement with galvanneal coating requirements [24].

As  $w_c\sigma_c$  decreases, it can be observed how  $\tilde{\sigma}_a$  converges towards the effective conductivity  $\tilde{\sigma}_b$  of bare steel plates predicted in Section III-A, with the coating no longer effective in reducing the interaction and therefore the dissipation in the ferromagnetic background. As a result, the transition region no longer scales with the frequency.

Fig. 11(f) is based on three separate data sets measured in the same facility, jointly spanning more than a decade, well agreeing with prediction from the multi-layer model. Fig. 11(h) is of particular interest, since it presents results spanning the widest frequency range, with the most detailed account of testing setup and conditions [81].

These results confirm that a wide transition region is a hallmark of GSP, explaining the high variability of its apparent conductivity, in particular the very poor conductivity observed at lower frequencies. Moreover, the fact that  $w_c\sigma_c$  can change more than tenfold compounds this variability. It is remarkable that these results can be explained on the basis of the physical properties of the four constituents of galvanizing coatings, taking into account technological constraints and results from zinc metallurgy, as described in Section II. The main advantage of this approach is its ability in restricting the range of potential coating structures and therefore a GSP apparent conductivity, while still explaining the wide variability in the apparent conductivity. By doing so it also provides clear guidelines in estimating the worst-case conductivity that should be expected for a GSP and how it can be improved by avoiding coating technologies that

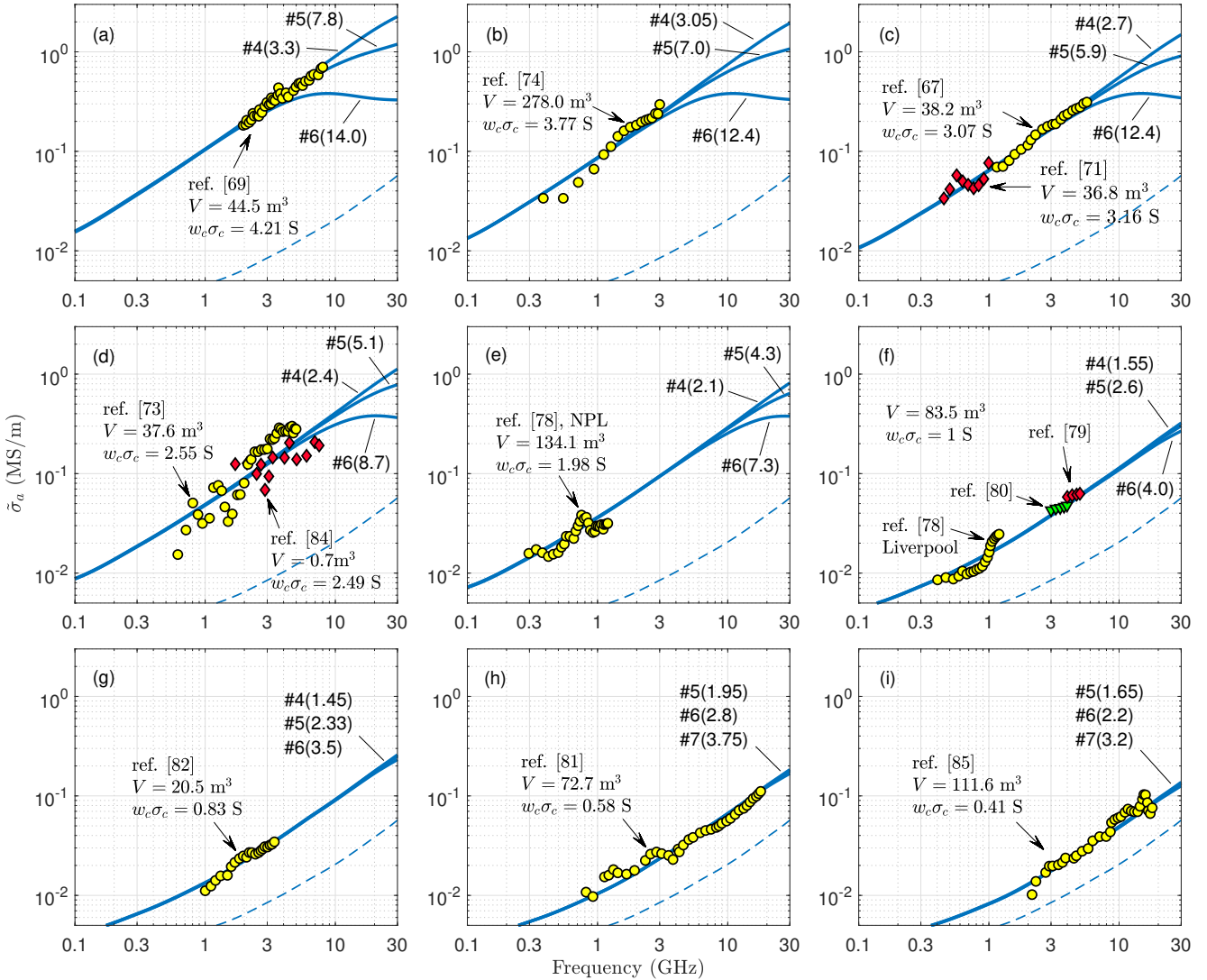


FIGURE 11: Apparent dissipative conductivity estimated from RC literature data, all results refer to GSP based cavities. References from which the data were extracted are shown in each figure, together with the volume of the RC. Solid lines are theoretical results based on the multi-layer model described in Section III-C, for some of the coating structures described in Table 2, for the thickness indicated in parenthesis. The results expected for a bare steel plate are shown as reference as a dashed line.

generate significant fractions of iron-zinc compounds.

### V. CONCLUSIONS

The pure zinc used for coating steel plates could be expected to ensure a high surface conductivity, close to 16.7 MS/m, but in fact galvanized steel plates (GSP) have been shown to present surprisingly poor conductivities, well short of 1 MS/m, i.e., lower than stainless steel [1], [87]. Adding further confusion, widely different results have been reported in the past depending on the coating technology and tested frequency.

The physical reasons for these observations were explored, first by gathering findings from materials science literature,

highlighting how metallurgy processes can transform zinc into poorly conductive iron-zinc compounds. Modeling the layered structures typical of GSP has led to predicting that their apparent conductivity increases with the frequency, while resulting in very poor conductivity at low frequency, ranging in the tens of kS/m for  $w_c\sigma_c < 1$  S. These results have also proven that surface roughness is not the main physical mechanism behind low conductivity in bare steel plates and GSP.

An extensive analysis of wide-band measurements from reverberation-chamber literature confirmed the transition region as a hallmark of the apparent conductivity of GSP, as well as the large variability in their coating features.

Galvannealed coatings appeared to be the most likely cause of the worst conductivity results observed in the past, because of a prevalence of  $\delta$  compound, indicating that this corrosion protection technology should be avoided when low losses are required.

The ability to predict the dissipation by GSP implies that these results can be used in order to better select the most suitable coating technology ensuring at the same time a satisfying corrosion protection and low dissipation. In fact, the proposed model proves that these two goals are not mutually exclusive, but rather that the coating technology and thickness must be selected carefully, depending on the frequency of use for microwave applications. Given that the transition region inevitably results in increasing dissipation in the steel background at low frequency, it may be more effective to switch to alternative structural steel solutions, such as austenitic stainless steels, which present 1-3 MS/m conductivity even at low frequency. Clearly, a much better conductivity can be achievable above 1 GHz by using non-annealed GSP, with a coating just a few micron thick.

The opposite objective of purposely selecting a GSP coating technology to ensure lower conductivities can also be envisaged. This can be useful in wireless applications in closed reverberating environments, where introducing higher dissipation would be seen as a first-resort solution to limit time spreading in wireless communications.

## APPENDIX A DISSIPATION IN BULK MAGNETIC METALS

As seen in Section III-A, the reflectivity of a steel half-space has the structure  $\Gamma_b = -1 + x$ , where  $x = 2 \cos \theta_i \sqrt{j\omega\epsilon_0/\sigma'_b}$ . Hence  $1 - |\Gamma_b|^2 = 2\text{Re } x - |x|^2$  and since  $\text{Re } x \gg |x|^2$

$$1 - |\Gamma_b|^2 \simeq 4 \cos \theta_i \sqrt{\omega\epsilon_0 \tilde{\mu}_b / 2\sigma_b} \quad (24)$$

given that for a complex number  $z$ , its principle value root has  $\text{Re}\sqrt{z} = \sqrt{(|z| + \text{Re } z)/2}$ . The effective dissipative permeability  $\tilde{\mu}_b = |\mu_b| + \mu_b''$  models the additional losses introduced by steel's ferromagnetic response.

The quantity  $\tilde{\mu}_b$  also appears in the steel skin depth  $\delta_b$ . Given that the propagation constant  $k_b$  has  $k_b^2 = -j\omega\mu_0\mu_b\sigma_b$ , and that  $\delta_b = -1/\text{Im } k_b$ ,

$$\delta_b = \delta_o / \sqrt{\tilde{\mu}_b} = \sqrt{2/\omega\mu_0\tilde{\mu}_b\sigma_b} \quad (25)$$

where  $\delta_o$  is the skin depth expected for  $\mu_b = 1$ .

## APPENDIX B UNCERTAINTY OF $\tilde{\sigma}_A$ ESTIMATES

A statistical description of the uncertainty is adopted, approximating each quantity as a Gaussian random variable, unless stated otherwise. The normalized standard deviation, relative to the estimated (average) value, is marked as  $\epsilon$ .

The data sets deal with the composite quality factor  $Q$  of RC, which is evaluated from  $N_s$  ideally independent realizations, generated by means of stirring techniques [88]. Detailed uncertainty budgets for  $Q$  have been reported in [58], [89]; for power transmission-based estimates of  $Q$ , its normalized standard deviation is approximatively equal to

$\epsilon(Q) \sim 1/\sqrt{N_s}$ . For a typical configuration with  $N_s = 100$ ,  $\epsilon(Q) \simeq 0.1$ .

Another source of uncertainty is the antenna-loss factor  $Q_a$ , whose computation from (20) requires knowledge of the mismatch factor  $m = 1 - \eta_a^2 |\Gamma_a|^2$ . For an input antenna with  $|\Gamma_a| = -10$  dB and  $\eta_a \in [0.7, 1]$ ,  $m \in [0.90, 0.95]$ . Assuming a uniform distribution over this range, the standard deviation is  $0.05/\sqrt{12}$ , hence  $\epsilon(m) \simeq 0.016$ .

Finally, the volume  $V$  and the overall metallic surface  $S$  of an RC are also uncertain. The inner walls are not perfectly flat, due to the presence of bolted/riveted butt joints used for joining adjacent metal plates, typically a few millimeters thick. The dimensions described in the literature instead correspond to the linear distance between opposite facing surfaces. A upper bound of a 0.5% normalized standard deviation for each cavity width will be considered, based on the two RC available at our institution.

Applying standard propagation of uncertainty [90] to (22), the normalized standard deviation of  $\tilde{\sigma}_a$  can be expressed as

$$\frac{\epsilon^2(\tilde{\sigma}_a)}{4} = \left[ \frac{\epsilon(Q)}{1 - Q/Q_a} \right]^2 + \left[ \frac{\epsilon(m)}{1 - Q_a/Q} \right]^2 + \epsilon^2(V) + \epsilon^2(S). \quad (26)$$

The first term's contribution is significantly amplified for  $Q_a \sim Q$ , which is expected to occur in the lower frequency range of use of a RC, typically below 1 GHz. In order to keep this phenomenon in check, only frequencies high enough to ensure that  $Q_a/Q > 3$  were considered in Section IV. Since  $Q_a/Q = Q_a/Q_w + 1$ , the previous condition requires that power dissipation over the RC inner metal surface is at least twice that leaking through antennas. This same condition reduces the already minor contribution from the second term, i.e., from antenna-related dissipation, leaving the first term as the main contributor to uncertainty, with  $\epsilon(\tilde{\sigma}_a) \simeq 3\epsilon(Q)$  as a worst case in the lower frequency range. As an example, results based on 100 independent samples of  $Q$  would lead to an upper bound  $\epsilon(\tilde{\sigma}_a) \simeq 0.3$ , i.e., an expanded relative uncertainty at worst around  $\pm 60\%$ , for a 95% coverage. As  $Q_a/Q$  increases, this result asymptotically reduces to  $\pm 40\%$ .

## REFERENCES

- [1] C. Moosbrugger, *ASM ready reference: electrical and magnetic properties of metals*. ASM International, 2000.
- [2] E. Maxwell, "Conductivity of metallic surfaces at microwave frequencies," *Journal of Applied Physics*, vol. 18, no. 7, pp. 629–638, 1947.
- [3] F. Benson, "Attenuation in nickel and mild-steel waveguides at 9375 mc/s," *Proceedings of the IEE-Part III: Radio and Communication Engineering*, vol. 101, no. 69, pp. 38–41, 1954.
- [4] T. Y. Otoshi and M. M. Franco, "The electrical conductivities of steel and other candidate materials for shrouds in a beam-waveguide antenna system," *IEEE Trans. Instrum. Meas.*, vol. 45, no. 1, pp. 77–83, Feb 1996.
- [5] G. Tait, M. Slocum, and R. Richardson, "On multipath propagation in electrically large reflective spaces," *IEEE Antennas Wireless Propag. Lett.*, vol. 8, pp. 232–235, 2009.
- [6] D. A. Hill, *Electromagnetic fields in cavities: deterministic and statistical theories*. John Wiley & Sons, 2009.
- [7] P. Besnier and B. Démoulin, *Electromagnetic reverberation chambers*. John Wiley & Sons, 2013.
- [8] C. Bruns and R. Vahldieck, "A closer look at reverberation chambers - 3D simulation and experimental verification," *IEEE Trans. Electromagn. Compat.*, vol. 47, no. 3, pp. 612–626, 2005.

- [9] A. Cozza and F. Monsef, "Power dissipation in reverberation chamber metallic surfaces based on ferrous materials," *IEEE Trans. Electromagn. Compat.*, vol. 61, no. 6, pp. 1714–1725, 2018.
- [10] N. L. Okamoto, M. Inomoto, H. Takebayashi, and H. Inui, "Crystal structure refinement of the  $\Gamma$ - and  $\Gamma_1$ -phase compounds in the Fe-Zn system and orientation relationships among  $\alpha$ -Fe,  $\Gamma$  and  $\Gamma_1$  phases in the coating layer of galvanized steel," *Journal of Alloys and Compounds*, vol. 732, pp. 52–63, 2018.
- [11] R. Lynch, "Zinc: Alloying, thermomechanical processing, properties, and applications," in *Encyclopedia of Materials: Science and Technology*, K. J. B. et al., Ed. Oxford: Elsevier, 2001, pp. 9869–9883.
- [12] A. Marder, "The metallurgy of zinc-coated steel," *Progress in materials science*, vol. 45, no. 3, pp. 191–271, 2000.
- [13] American Galvanizers Association, "Zinc coatings," available from [http://courtagalvanizinginc.com/wp-content/uploads/2012/04/Zinc\\_Coatings.pdf](http://courtagalvanizinginc.com/wp-content/uploads/2012/04/Zinc_Coatings.pdf), 2012.
- [14] International Zinc Association, "The continuous electroplating process for steel sheet products," available from <https://www.galvinfo.com/galvinfonotes/>, 2017.
- [15] V. Kuklík and J. Kudlacek, *Hot-dip galvanizing of steel structures*. Butterworth-Heinemann, 2016.
- [16] P. Pokorný, J. Kolisko, L. Balík, and P. Novák, "Reaction kinetics of the formation of intermetallic Fe–Zn during hot-dip galvanizing of steel," *Metallurgija*, vol. 55, no. 1, pp. 111–114, 2016.
- [17] C. Allen, "A study of the interaction of solid iron with liquid zinc," Ph.D. dissertation, University of Surrey (United Kingdom), 1963.
- [18] International Zinc Association, "The role of aluminum in continuous hot-dip galvanizing," available from <https://www.galvinfo.com/galvinfonotes/>, 2019.
- [19] —, "Continuous hot-dip galvanizing versus general (batch) galvanizing," available from <https://www.galvinfo.com/galvinfonotes/>, 2017.
- [20] C. E. Jordan and A. Marder, "Morphology development in hot-dip galvanneal coatings," *Metallurgical Transactions, A (Physical Metallurgy and Materials Science)*, vol. 25, no. 5, 1994.
- [21] O. Ighodaro, "Effects of metallic coatings on resistance spot weldability of hot stamping steel," Master's thesis, University of Waterloo (Canada), 2017.
- [22] International Zinc Association, "55% aluminum-zinc alloy-coated steel sheet," available from <https://www.galvinfo.com/galvinfonotes/>, 2017.
- [23] Z. Liu and O. N. Uwakweh, "Mössbauer effect study of mechanically alloyed  $\Gamma$  and  $\Gamma_1$  Fe–Zn intermediate phases," *Metallurgical and Materials Transactions A*, vol. 28, no. 13, pp. 743–747, 1997.
- [24] International Zinc Association, "Galvanneal: Differences from galvanize," available from <https://www.galvinfo.com/galvinfonotes/>, 2018.
- [25] I. H. Karahan, "A study on electrodeposited  $Zn_{1-x}Fe_x$  alloys," *Journal of Materials Science*, vol. 42, no. 24, pp. 10 160–10 163, 2007.
- [26] G. Banerjee, T. K. Pal, N. Bandyopadhyay, and D. Bhattacharjee, "Effect of welding conditions on corrosion behaviour of spot welded coated steel sheets," *Corrosion Engineering, Science and Technology*, vol. 46, no. 1, pp. 64–69, 2011.
- [27] S. Chatterjee, S. Koley, R. B. Sarkar, N. Behera, M. Manna, S. Mukherjee, and S. Kundu, "Design and development of galvanneal dual-phase steel: Microstructure, mechanical properties and weldability," *Journal of Materials Engineering and Performance*, vol. 28, no. 1, pp. 231–241, 2019.
- [28] D. C. Cook and R. G. Grant, "Iron-zinc intermetallics in commercial galvanneal steel coatings," in *Mössbauer Spectroscopy Applied to Magnetism and Materials Science*, G. J. Long and F. Grandjean, Eds. Boston, MA: Springer US, 1996, pp. 225–271.
- [29] R. G. Grant, P. S. Cook, and D. C. Cook, "Preparation and chemical analysis of high purity iron-zinc alloys," *Journal of Materials Research*, vol. 10, no. 10, pp. 2454–2462, 1995.
- [30] R. G. Grant, "Identification and characterization of the iron-intermetallics formed in galvanneal steel." Ph.D. dissertation, Old Dominion University (United States), 1995.
- [31] G. T. Meaden, *Electrical resistance of metals*. Springer, 2013.
- [32] C. Y. Ho, M. Ackerman, K. Wu, T. Havill, R. Bogaard, R. Matula, S. Oh, and H. James, "Electrical resistivity of ten selected binary alloy systems," *Journal of Physical and Chemical Reference Data*, vol. 12, no. 2, pp. 183–322, 1983.
- [33] J. B. Dunlop, "Electronic properties of some zinc-transition metal compounds," Ph.D. dissertation, Imperial College London (United Kingdom), 1972.
- [34] S. Jazbec, P. Koželj, S. Vrtnik, Z. Jagličič, P. Popčević, J. Ivkov, D. Stanić, A. Smontara, M. Feuerbacher, and J. Dolinšek, "Electrical, magnetic, and thermal properties of the  $\delta$  – FeZn<sub>10</sub> complex intermetallic phase," *Physical Review B*, vol. 86, no. 6, p. 064205, 2012.
- [35] N. Gross, G. Kotzyba, B. Künne, and W. Jeitschko, "Binary compounds of rhodium and zinc: RhZn, Rh<sub>2</sub>Zn<sub>11</sub>, and RhZn<sub>13</sub>," *Zeitschrift für Anorganische und Allgemeine Chemie*, vol. 627, no. 2, pp. 155–163, 2001.
- [36] J. Davis, *Metals handbook; desk edition*. American Society for Metals, Metals Park, OH, 1998.
- [37] R. Taylor, "Electron spin resonance studies of some magnetic alloys," Ph.D. dissertation, Imperial College London (United Kingdom), 1972.
- [38] A. Caplin and J. Dunlop, "Dilute intermetallic compounds: the properties of zinc transition metal  $\zeta$  phases," *Journal of Physics F: Metal Physics*, vol. 3, no. 8, p. 1621, 1973.
- [39] V. Parshin and S. Myasnikova, "Metals reflectivity at frequencies 100–360 GHz," in *2005 Joint 30th International Conference on Infrared and Millimeter Waves and 13th International Conference on Terahertz Electronics*, vol. 2. IEEE, 2005, pp. 569–570.
- [40] M. Kirley and J. H. Booske, "Terahertz conductivity of copper surfaces," *IEEE Transactions on Terahertz Science and Technology*, vol. 5, no. 6, pp. 1012–1020, 2015.
- [41] J. D. Cook, J. W. Zwart, K. J. Long, V. O. Heinen, and N. Stankiewicz, "An experimental apparatus for measuring surface resistance in the submillimeter-wavelength region," *Review of Scientific Instruments*, vol. 62, no. 10, pp. 2480–2485, 1991.
- [42] M. Dressel and M. Scheffler, "Verifying the Drude response," *Annalen der Physik*, vol. 15, no. 7–8, pp. 535–544, 2006.
- [43] N. Laman and D. Grischkowsky, "Terahertz conductivity of thin metal films," *Applied Physics Letters*, vol. 93, no. 5, p. 051105, 2008.
- [44] J. G. Van Bladel, *Electromagnetic fields*. Wiley-IEEE Press, 2007.
- [45] R. E. Hummel, *Electronic properties of materials*. Springer Science & Business Media, 2011.
- [46] E. A. Brandes and G. B. Brook, *Smithells metals reference book*. Butterworth-Heinemann, Oxford, 1992.
- [47] W. Haynes, *CRC Handbook of Chemistry and Physics*. Taylor & Francis Inc., Boca Raton, 2015.
- [48] R. Millership and F. V. Webster, "High frequency permeability of ferromagnetic materials," *Proceedings of the Physical Society. Section B*, vol. 63, no. 10, pp. 783–795, 1950.
- [49] C. Kittel, "Theory of the dispersion of magnetic permeability in ferromagnetic materials at microwave frequencies," *Physical Review*, vol. 70, no. 5–6, pp. 281–290, 1946.
- [50] J. Allison, F. Benson, and M. Seaman, "Characteristics of some ferrous and non-ferrous waveguides at 27 Gc/s," *Proceedings of the IEE-Part B: Radio and Electronic Engineering*, vol. 104, no. 18, pp. 599–602, 1957.
- [51] E. Thom and T. Otoshi, "Surface resistivity measurements of candidate subreflector surfaces," Jet Propulsion Laboratory, NASA, Tech. Rep., 1981.
- [52] T. Otoshi, M. Franco, and H. Reilly Jr, "The electrical conductivities of the dss-13 beam-waveguide antenna shroud material and other antenna reflector surface materials," Jet Propulsion Laboratory, NASA, Tech. Rep., 1992.
- [53] J. Dobrowolski, *Microwave network design using the scattering matrix*. Artech House, 2010.
- [54] H. E. Bussey, "Standards and measurements of microwave surface impedance, skin depth, conductivity and Q," *IRE Transactions on Instrumentation*, vol. I-9, no. 2, pp. 171–175, 1960.
- [55] Y. Dong, M. S. Jellesen, R. J. Christiansen, J. Høvelskov, J. Sundgren, and K. B. Jakobsen, "Electrical conductivity measurement on metallic materials with a cylindrical resonator," *IEEE Trans. Electromagn. Compat.*, 2021, in press.
- [56] F. Costa, M. Borgese, M. Degiorgi, and A. Monorchio, "Electromagnetic characterisation of materials by using transmission/reflection devices," *Electronics*, vol. 6, no. 4, p. 95, 2017.
- [57] B. Liu, D. Chang, and M. Ma, "Eigenmodes and the composite quality factor of a reverberating chamber," *US Nat. Bur. Stand. Tech. Note*, vol. 1066, 1983.
- [58] J. Kostas and B. Boverie, "Statistical model for a mode-stirred chamber," *IEEE Trans. Electromagn. Compat.*, vol. 33, no. 4, pp. 366–370, 1991.
- [59] A. Cozza, "The role of losses in the definition of the overmoded condition for reverberation chambers and their statistics," *IEEE Trans. Electromagn. Compat.*, vol. 53, no. 2, pp. 296–307, May 2011.

- [60] D. Hill, "Plane wave integral representation for fields in reverberation chambers," *IEEE Trans. Electromagn. Compat.*, vol. 40, no. 3, pp. 209–217, 1998.
- [61] *Testing and measurement techniques - Reverberation chamber test methods*, International Electrotechnical Commission (IEC) Std. 61 000-4-21, 2011.
- [62] D. Hill, "Electromagnetic Theory of Reverberation Chambers," National Institute of Standards and Technology, Tech. Rep. 1506, 1998.
- [63] A. Cozza, "Power loss in reverberation chambers by antennas and receivers," *IEEE Trans. Electromagn. Compat.*
- [64] I. Junqua, P. Degauque, M. Liñard, and F. Issac, "On the power dissipated by an antenna in transmit mode or in receive mode in a reverberation chamber," *IEEE Trans. Electromagn. Compat.*, vol. 54, no. 1, pp. 174–180, Feb 2012.
- [65] C. Bruns, "Three-dimensional simulation and experimental verification of a reverberation chamber," Ph.D. dissertation, ETH Zurich (Switzerland), 2005.
- [66] C. Holloway, D. Hill, J. Ladbury, P. Wilson, G. Koepke, and J. Coder, "On the use of reverberation chambers to simulate a rician radio environment for the testing of wireless devices," *IEEE Trans. Antennas Propag.*, vol. 54, no. 11, pp. 3167–3177, Nov 2006.
- [67] C. L. Holloway, H. A. Shah, R. J. Pirkl, W. F. Young, D. A. Hill, and J. Ladbury, "Reverberation chamber techniques for determining the radiation and total efficiency of antennas," *IEEE Trans. Antennas Propag.*, vol. 60, no. 4, pp. 1758–1770, April 2012.
- [68] D. L. Green, V. Rajamani, C. F. Bunting, B. Archambeault, and S. Connor, "One-port time domain measurement technique for quality factor estimation of loaded and unloaded cavities," in *2013 IEEE International Symposium on Electromagnetic Compatibility*. IEEE, 2013, pp. 747–750.
- [69] H. Vallon, A. Chauchat, F. Monsef, and A. Cozza, "Effect of loading a mode-stirred chamber with antennas on Q-factor and comparison to theory," in *2014 XXXIth URSI General Assembly and Scientific Symposium (URSI GASS)*. IEEE, 2014, pp. 1–4.
- [70] L. R. Arnaut, F. Moglie, L. Bastianelli, and V. M. Primiani, "Helical stirring for enhanced low-frequency performance of reverberation chambers," *IEEE Trans. Electromagn. Compat.*, vol. 59, no. 4, pp. 1016–1026, 2017.
- [71] H.-J. Asander, G. Eriksson, L. Jansson, and H. Akermark, "Field uniformity analysis of a mode stirred reverberation chamber using high resolution computational modeling," in *2002 IEEE International Symposium on Electromagnetic Compatibility*, vol. 1. IEEE, 2002, pp. 285–290.
- [72] K. R. Goldsmith and P. A. Johnson, "Design, construction, computational EM modelling, and characterisation of an aircraft sized reverberation chamber and stirrer," in *Proceedings of the 17th Digital Avionics Systems Conference*. IEEE, 1998, pp. D55 1–8.
- [73] O. Lundén and M. Bäckström, "Absorber loading study in FOI 36.7 m<sup>3</sup> mode stirred reverberation chamber for pulsed power measurements," in *IEEE EMC Symposium, Detroit, USA*, 18-22 August 2008.
- [74] J. Yousaf, W. Nah, M. I. Hussein, J. G. Yang, A. Altaf, and M. Elahi, "Characterization of reverberation chambers - a comprehensive review," *IEEE Access*, vol. 8, pp. 226 591–226 608, 2020.
- [75] I. D. Flintoft, S. J. Bale, S. L. Parker, A. C. Marvin, J. F. Dawson, and M. P. Robinson, "On the measurable range of absorption cross section in a reverberation chamber," *IEEE Trans. Electromagn. Compat.*, vol. 58, no. 1, pp. 22–29, 2015.
- [76] L. R. Arnaut, M. I. Andries, J. Sol, and P. Besnier, "Evaluation method for the probability distribution of the quality factor of mode-stirred reverberation chambers," *IEEE Trans. Antennas Propag.*, vol. 62, no. 8, pp. 4199–4208, 2014.
- [77] P. Besnier, C. Lemoine, and J. Sol, "Various estimations of composite Q-factor with antennas in a reverberation chamber," in *2015 IEEE International Symposium on Electromagnetic Compatibility (EMC)*, Aug 2015, pp. 1223–1227.
- [78] C. Li, T.-H. Loh, Z. H. Tian, Q. Xu, and Y. Huang, "A comparison of antenna efficiency measurements performed in two reverberation chambers using non-reference antenna methods," in *2015 Loughborough Antennas & Propagation Conference (LAPC)*. IEEE, 2015, pp. 1–5.
- [79] Z. Tian, Y. Huang, Y. Shen, and Q. Xu, "Efficient and accurate measurement of absorption cross section of a lossy object in reverberation chamber using two one-antenna methods," *IEEE Trans. Electromagn. Compat.*, vol. 58, no. 3, pp. 686–693, 2016.
- [80] Q. Xu, Y. Huang, X. Zhu, L. Xing, Z. Tian, and C. Song, "A modified two-antenna method to measure the radiation efficiency of antennas in a reverberation chamber," *IEEE Antennas Wireless Propag. Lett.*, vol. 15, pp. 336–339, 2015.
- [81] L. Bronckers, A. Roc'h, and A. Smolders, "Reverberation chamber enhanced backscattering: High-frequency effects," in *2019 International Symposium on Electromagnetic Compatibility - EMC EUROPE*, 2019, pp. 1–6.
- [82] W. Krouka, F. Sarrazin, and E. Richalot, "Influence of the reverberation chamber on antenna characterization performances," in *2018 International Symposium on Electromagnetic Compatibility (EMC EUROPE)*. IEEE, 2018, pp. 329–333.
- [83] S. F. Romero, G. Gutierrez, and I. Gonzalez, "Prediction of the maximum electric field level inside a metallic cavity using a quality factor estimation," *Journal of Electromagnetic Waves and Applications*, vol. 28, no. 12, pp. 1468–1477, 2014.
- [84] R. E. Richardson, "Reverberant microwave propagation," Naval Surface Warfare Center Dahl Gren Div. VA, Tech. Rep., 2008.
- [85] M. Añón-Cancela, D. Hernández-Gómez, M. Vázquez-Pascual, and D. López-Sanz, "Radiated susceptibility tests in thermal vacuum chambers for space systems," in *2016 ESA Workshop on Aerospace EMC*, 2016, pp. 1–4.
- [86] D. Hill, M. Ma, A. Ondrejka, B. Riddle, M. Crawford, and R. Johnk, "Aperture excitation of electrically large, lossy cavities," *IEEE Trans. Electromagn. Compat.*, vol. 36, no. 3, pp. 169–178, 1994.
- [87] A. Clark, G. Childs, and G. Wallace, "Electrical resistivity of some engineering alloys at low temperatures," *Cryogenics*, vol. 10, no. 4, pp. 295–305, 1970.
- [88] R. Serra, A. C. Marvin, F. Moglie, V. M. Primiani, A. Cozza, L. R. Arnaut, Y. Huang, M. O. Hatfield, M. Klingler, and F. Leferink, "Reverberation chambers a la carte: An overview of the different mode-stirring techniques," *IEEE Electromagnetic Compatibility Magazine*, vol. 6, no. 1, pp. 63–78, First 2017.
- [89] K. A. Remley, R. J. Pirkl, H. A. Shah, and C.-M. Wang, "Uncertainty from choice of mode-stirring technique in reverberation-chamber measurements," *IEEE Trans. Electromagn. Compat.*, vol. 55, no. 6, pp. 1022–1030, 2013.
- [90] Joint Committee for Guides in Metrology, "Evaluation of measurement data - Guide to the expression of uncertainty in measurement," 2008.



ANDREA COZZA (S'02 - M'05 - SM'12) received the Laurea degree in electronic engineering from Politecnico di Torino, Turin, Italy, in 2001 and the Ph.D. degree in electronics engineering jointly from Politecnico di Torino and University of Lille, France, in 2005. In 2007, he joined SUPELEC (now CentraleSupélec), Gif sur Yvette, France, where since 2013 he is Full Professor. He conducts his research activities at GeePs, the Group of Electrical Engineering of Paris, Gif sur

Yvette, France.

His current research interests include reverberation chambers, statistical electromagnetics, wave propagation through complex media, fault location techniques in transmission lines and applications of time reversal to electromagnetics.

Mr. Cozza's awards and honors include the 2012 Prix Coron-Thévenet (Académie des Sciences) and the 2019 Richard B. Schulz Best Transaction Paper Award (IEEE Transactions on Electromagnetic Compatibility).

...